

CHAPTER 4

RESULTS AND DISCUSSION

4.1 CuS synthesized via direct current heating

Figure 4.1 and Table 4.1 are the representative XRD spectra of the products produced for different lengths of time were specified that they are covellite CuS of JCPDS database (reference code: 06-0464) [80]. No other characteristic peaks of impurities, such as CuO and Cu₂S, were detected. For 1 s heating, the spectrum was rather broad. Peaks at $2\theta = 31.8\text{-}32.9^\circ$ were merged into a single one, showing that the product was composed of nanosized particles with low degree of crystallinity. The spectra became sharper and narrower when the length of time was longer, and the single broad peak split into two peaks – the (103) and (006) at 31.8° and 32.9° , respectively. For 3 min heating, the spectrum was the sharpest. At this stage, atoms were in lattice order and formed nanostructured CuS with the highest degree of crystallinity. The prolonged time has the influence on the phase formation by assisting Cu and S atoms in violent vibrating and diffusing at longer time. These atoms have more chance to reside in their normal lattices. The present research gives the yields (Table 4.2) of 87.9, 85.0, 84.6 wt % for the 1 s, 3 s, 5 s heating, respectively.

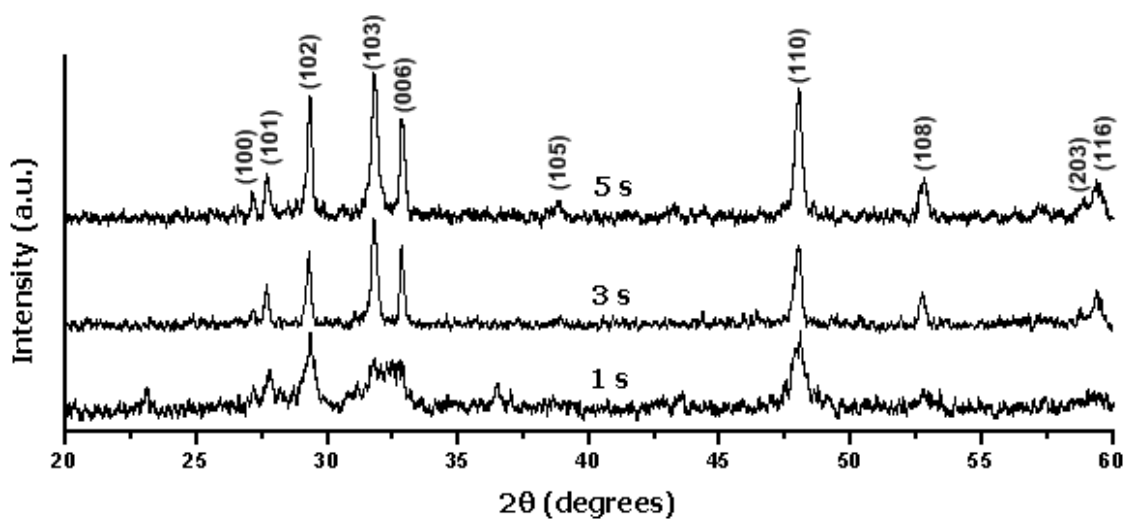


Figure 4.1 XRD spectra of the 1 s, 3 s and 5 s products.

Table 4.1 The 2θ diffraction angles (2θ) and intensities (I) of JCPDS no.06-0464 compare with experiments.

Plane	JCPDS		Experiment			
	code 06-0464		3 s		5 s	
	2θ	I (%)	2θ	I (%)	2θ	I (%)
(1 0 0)	27.12	14.00	27.18	24.72	27.13	29.52
(1 0 1)	27.68	30.00	27.68	40.52	27.66	37.30
(1 0 2)	29.28	65.00	29.22	55.79	29.33	88.24
(1 0 3)	31.79	100.00	31.77	100.00	31.79	100.00
(0 0 6)	32.85	55.00	32.85	71.59	32.85	71.64
(1 0 5)	38.84	10.00	-	-	38.82	21.49
(1 0 6)	43.10	6.00	-	-	-	-
(0 0 8)	44.30	8.00	-	-	-	-

Table 4.1 (continued)

Plane	JCPDS		Experiment			
	code 06-0464		3 s		5 s	
	2 θ	I (%)	2 θ	I (%)	2 θ	I (%)
(1 0 7)	47.78	25.00	-	-	-	-
(1 1 0)	47.94	75.00	47.94	82.67	47.94	82.73
(1 0 8)	52.72	35.00	52.71	30.50	52.78	36.43
(2 0 1)	56.25	4.00	-	-	-	-
(2 0 2)	57.21	8.00	-	-	-	-
(2 0 3)	58.68	16.00	58.72	21.07	58.84	24.21
(1 1 6)	59.35	35.00	59.38	34.75	59.38	34.77

Table 4.2 Calculated yields of products before and after synthesis.

Time (s)	Weight of Powder (g)		% Yields
	Before	After	
1	1.4213	1.2497	87.926
3	1.4214	1.2075	84.951
5	1.4215	1.2023	84.580

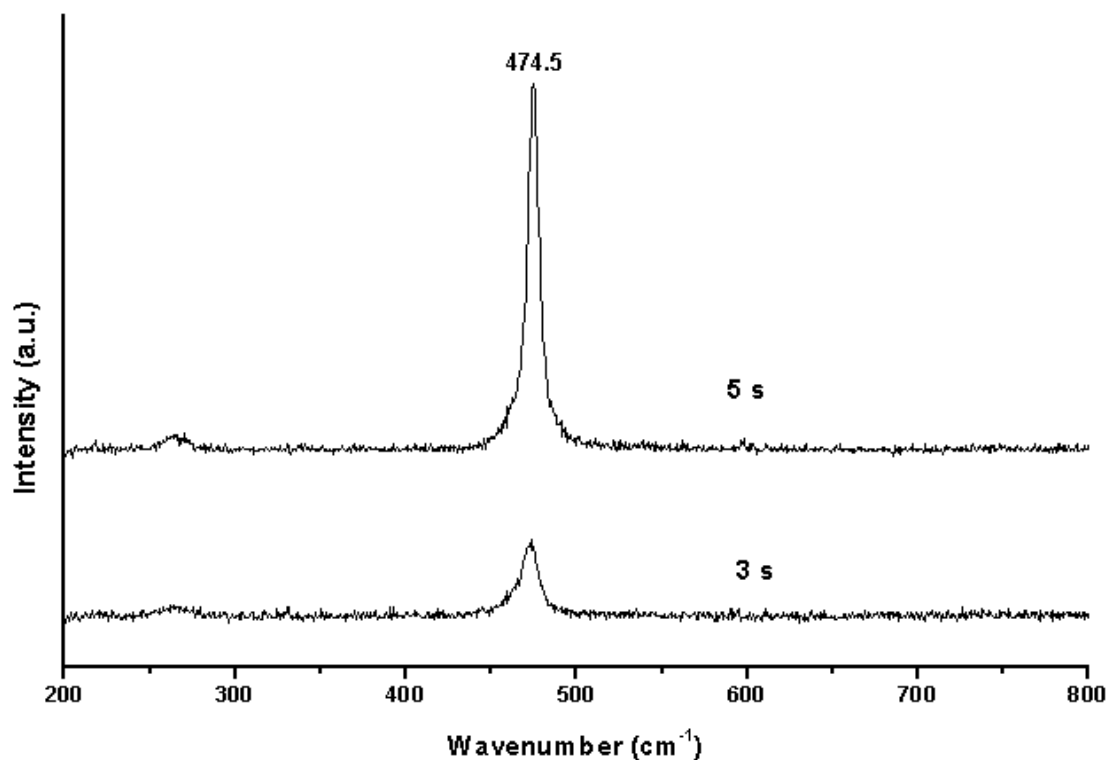


Figure 4.2 Raman spectra of CuS produced for 3 s and 5 s.

Figure 4.2, Raman spectra of CuS produced for 3 s and 5 s show that the vibration modes are in the same wavenumber at 474.5 cm^{-1} , corresponding to lattice vibrations [81]. The present results are in accordance with those characterized by Minceva-Sukarova et al. as a strong and sharp peak of CuS film at 474 cm^{-1} [81], and by Wang et al. of nanocrystalline CuS film with the size of 21.5 nm at 474 cm^{-1} [82]. It is worth noting that crystalline degree of the products has the influence on the peak intensity as well. For the 5 s product, its intensity is the strongest.

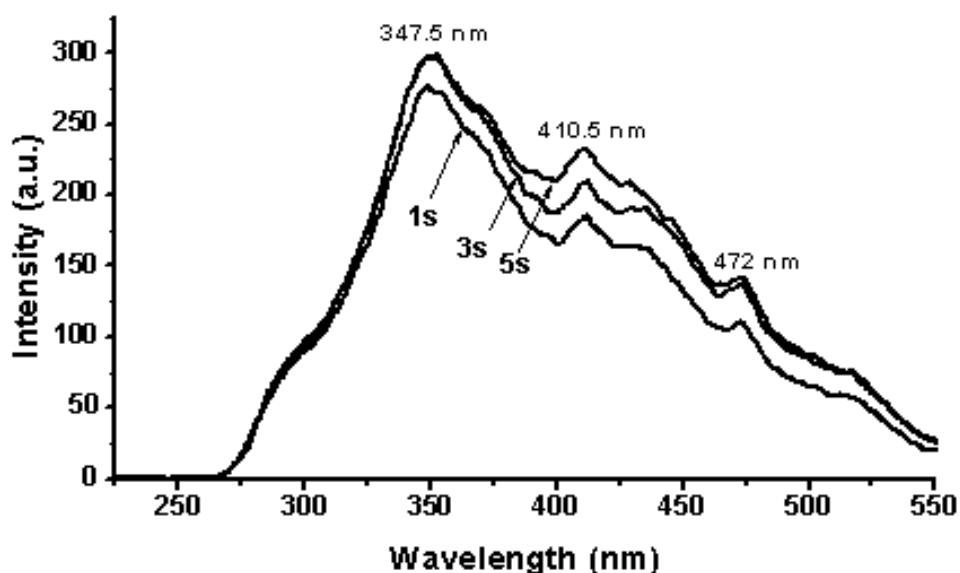
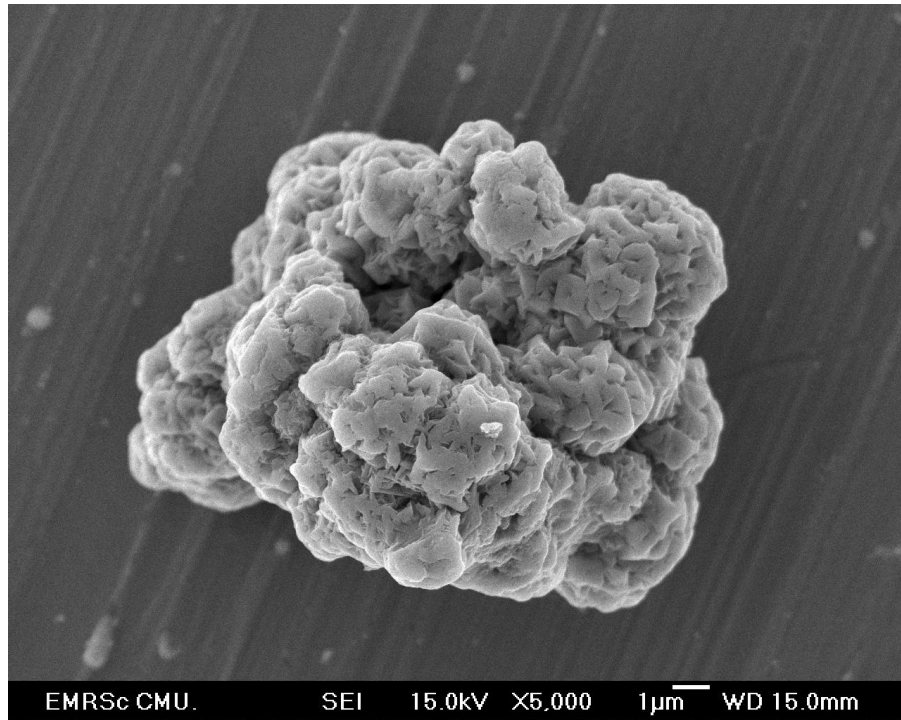
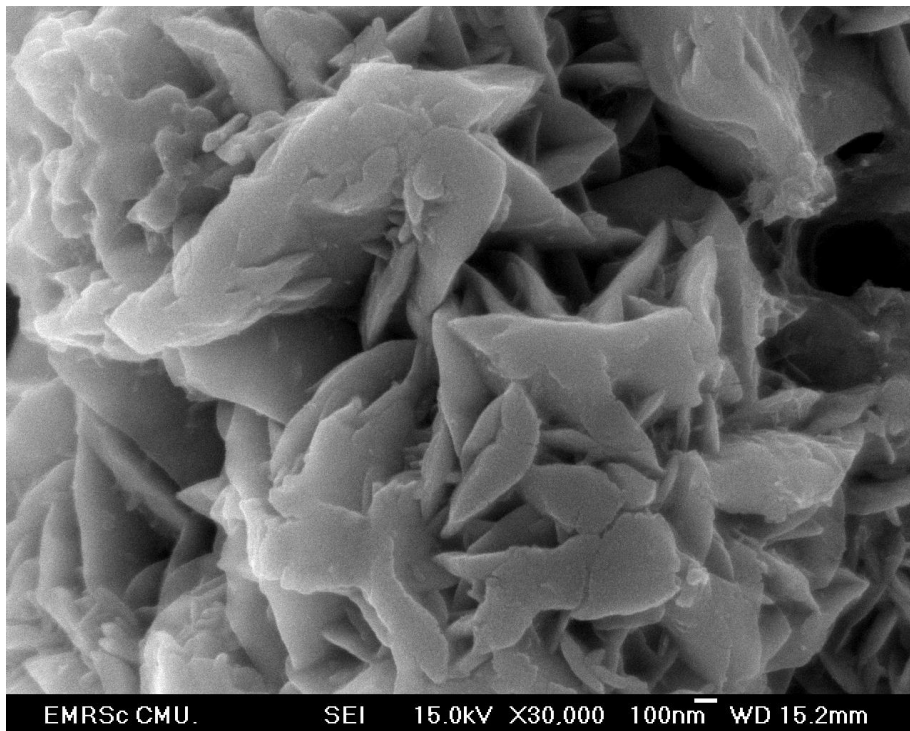


Figure 4.3 PL spectra of the products produced under different lengths of time.

PL emissions of solid CuS (Figure 4.3) were determined using a 202 nm excitation wavelength at room temperature. These emissions are at the same values of 347.5 nm with their shoulders at 410.5 nm and 472 nm. Comparing to the emission of CuS nanoplates at 339 nm determined by Zhang et al. [83], the present results are red-shift, caused by the morphological difference [84]. PL intensities were increased with the increase in the length of time. For the 5 s product, it is the best crystal and its PL intensity is the highest.

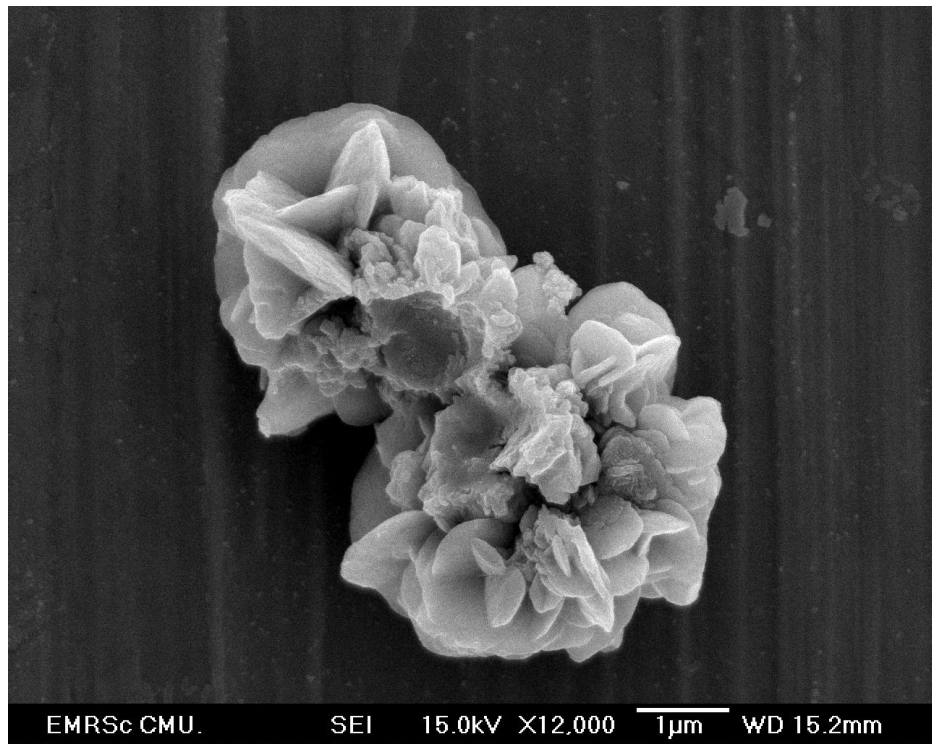


(a)

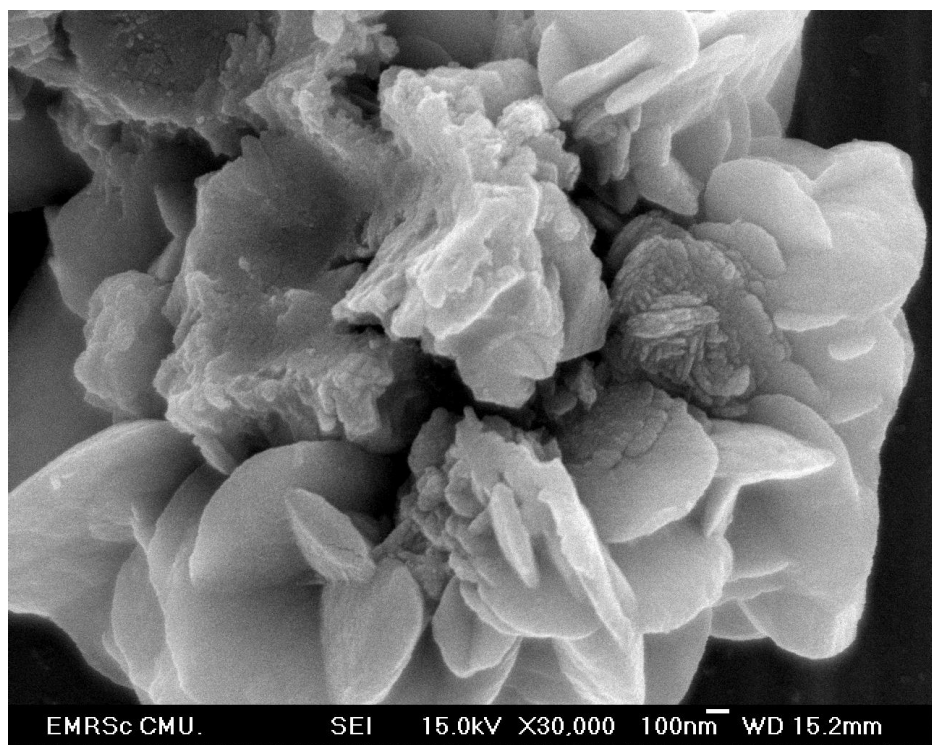


(b)

Figure 4.4 SEM image (a and b) of CuS produced for 1 s.

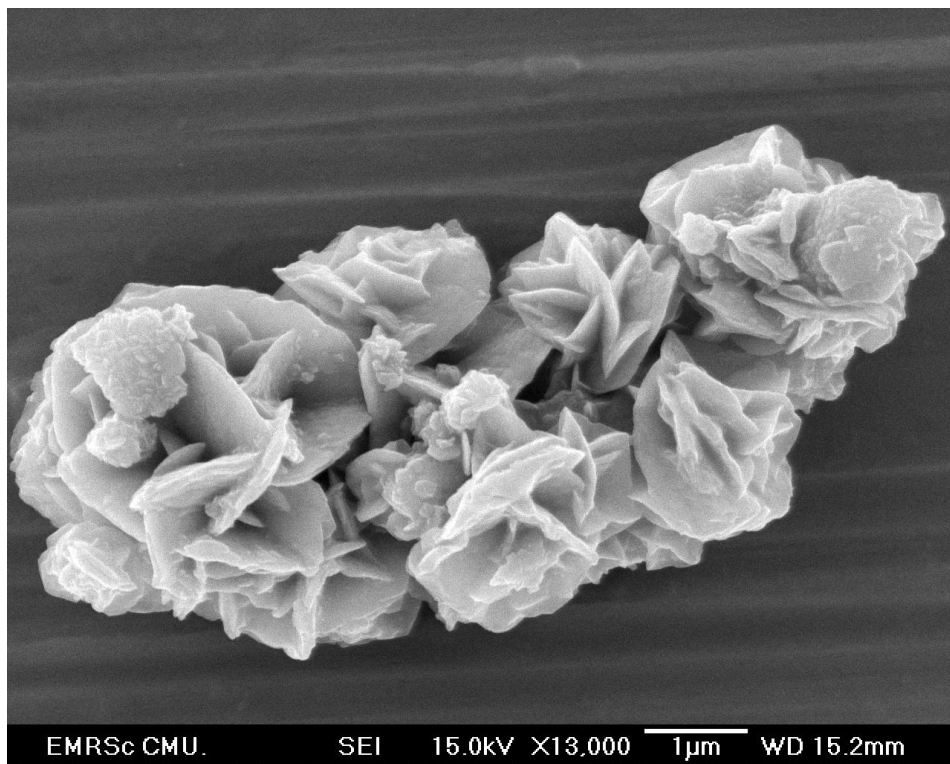


(a)

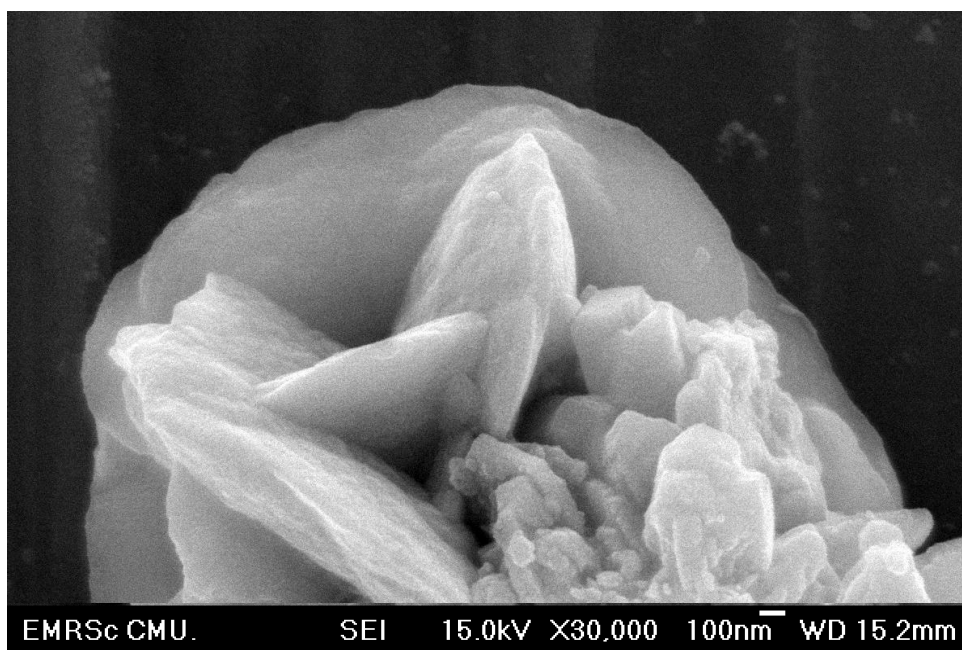


(b)

Figure 4.5 SEM image (a and b) of CuS produced for 3 s.



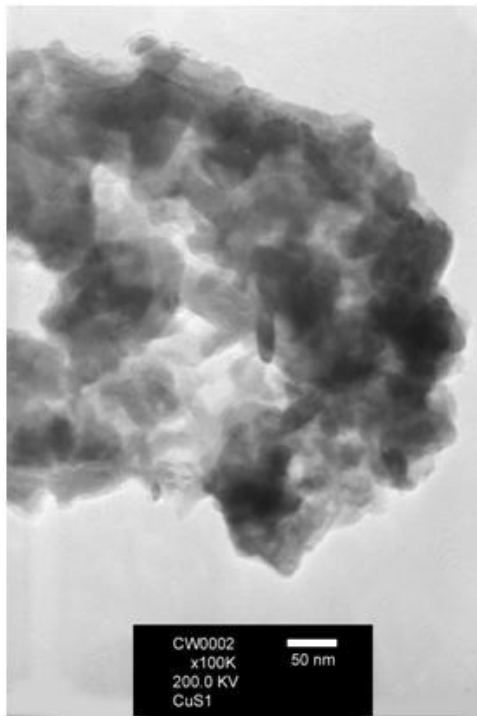
(a)



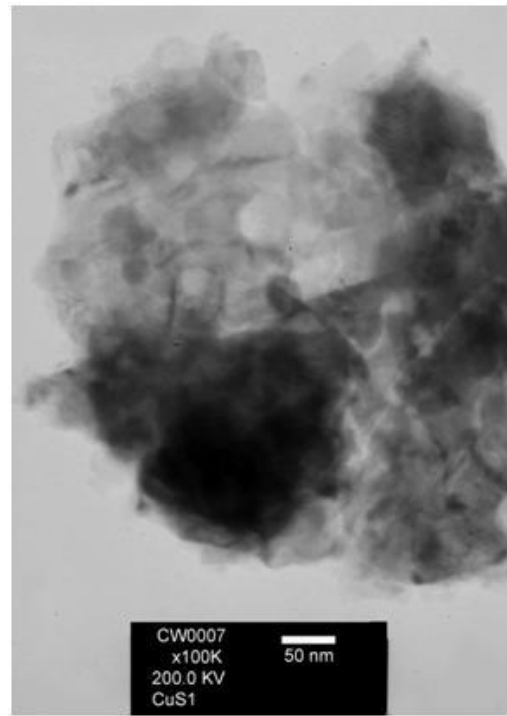
(b)

Figure 4.6 SEM image (a and b) of CuS produced for 5 s.

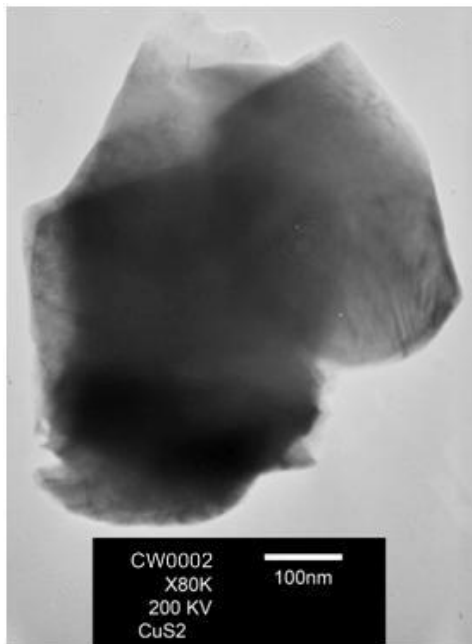
SEM images (Figures 4.4 - 4.6), TEM and HRTEM images (Figures 4.7 and 4.8) show different stages for the formation of nanostructured CuS flowers. For 1 s long, the product (Figures 4.4 and 4.7a and b) was nanostructured CuS, composing of a number of nanosized particles with different orientations. Then it transformed into the 1-2 μm nanostructured flowers by increasing the length of time. In part of incomplete (Figures 4.5) and complete (Figures 4.6) flowers for 3 s and 5 s, respectively. At these stages, several plates (Figures 4.5, 4.6, 4.7c and 4.8a) combined together to form a flower. Figures 4.7d and 4.8b shows SAED patterns of polycrystalline products produced for 3 s and 5 s, respectively. These diffraction patterns were composed of several concentric rings, corresponding to the planes of polycrystalline CuS with hexagonal structure of the JCPDS database [80]. For 5 s long, a set of parallel crystallographic planes (Figure 4.9b) with 0.85 nm space were detected. They are the (002) plane of covellite CuS phase [80], showing that these flowers are the best crystalline in nature. Electrical energy was directly supplied to the system composing of Cu and S powders to accelerate CuS (hcp) formation in vacuum. The length of time has very strong influence on the product morphologies and crystallinities.



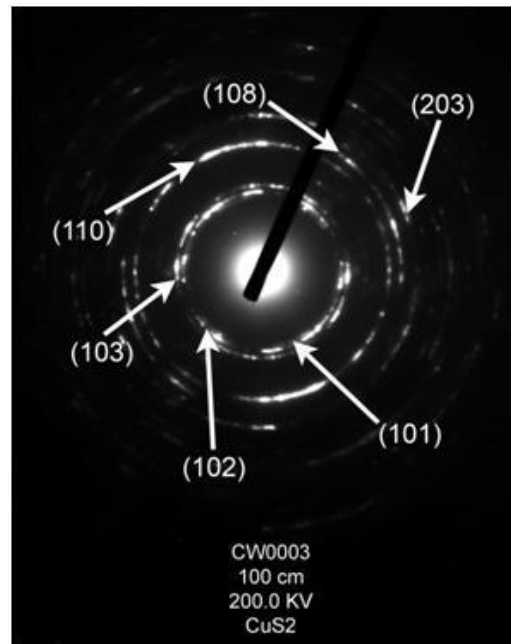
(a)



(b)



(c)



(d)

Figure 4.7 TEM images for 1 s (a and b), 3 s (c) and ring diffraction patterns of CuS produced for 3 s (d).

Table 4.3 Ring diffraction pattern values of CuS produced for 3 s.

Ring No.	Diameter (mm)	Radius (mm)	$d = L*\lambda/R$ (Å)	d (Å) (JCPDS file)	(hkl)
1	15.50	7.750	3.22103	3.22000	101
2	16.40	8.200	3.04427	3.04800	102
3	17.50	8.750	2.85291	2.81300	103
4	26.50	13.250	1.88400	1.89600	110
5	29.00	14.500	1.72159	1.73500	108
6	32.00	16.000	1.56019	1.57200	203

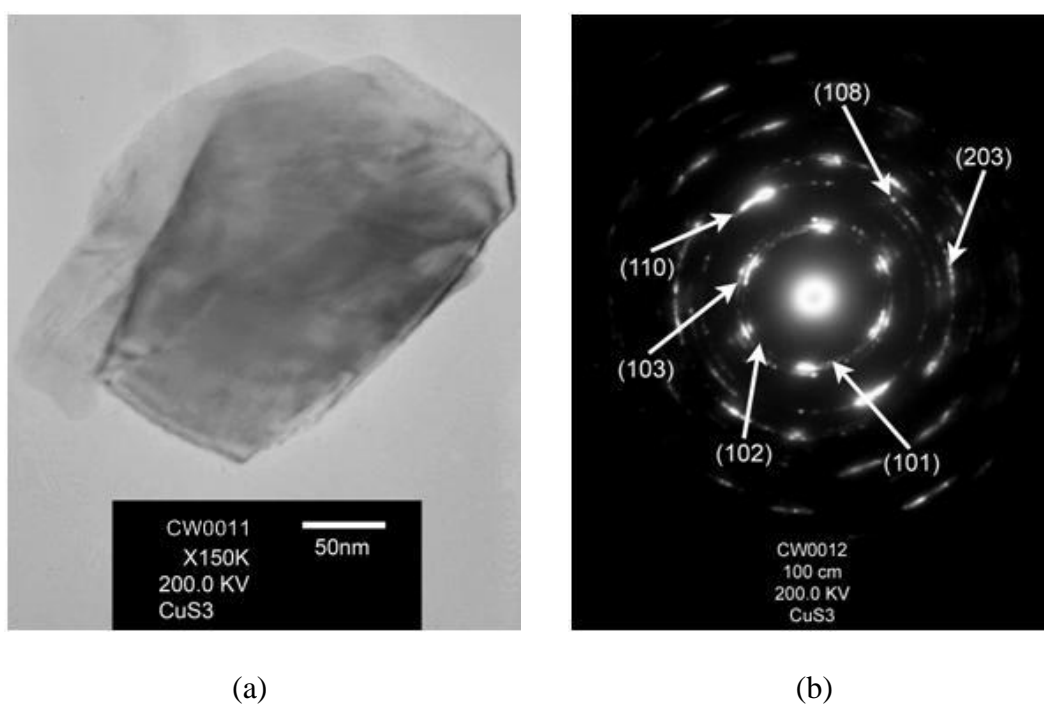


Figure 4.8 TEM images, and ring diffraction patterns of CuS for 5 s (a and b) respectively.

Table 4.4 Ring diffraction pattern values of CuS produced for 5 s.

Ring No.	Diameter (mm)	Radius (mm)	$d = L*\lambda/R$ (Å)	$d(\text{Å})$ (JCPDS file)	(hkl)
1	15.50	7.750	3.22103	3.22000	101
2	16.50	8.250	3.02582	3.04800	102
3	18.00	9.000	2.77367	2.81300	103
4	26.50	13.250	1.88400	1.89600	110
5	29.25	14.625	1.70687	1.73500	108
6	32.25	16.125	1.54809	1.57200	203

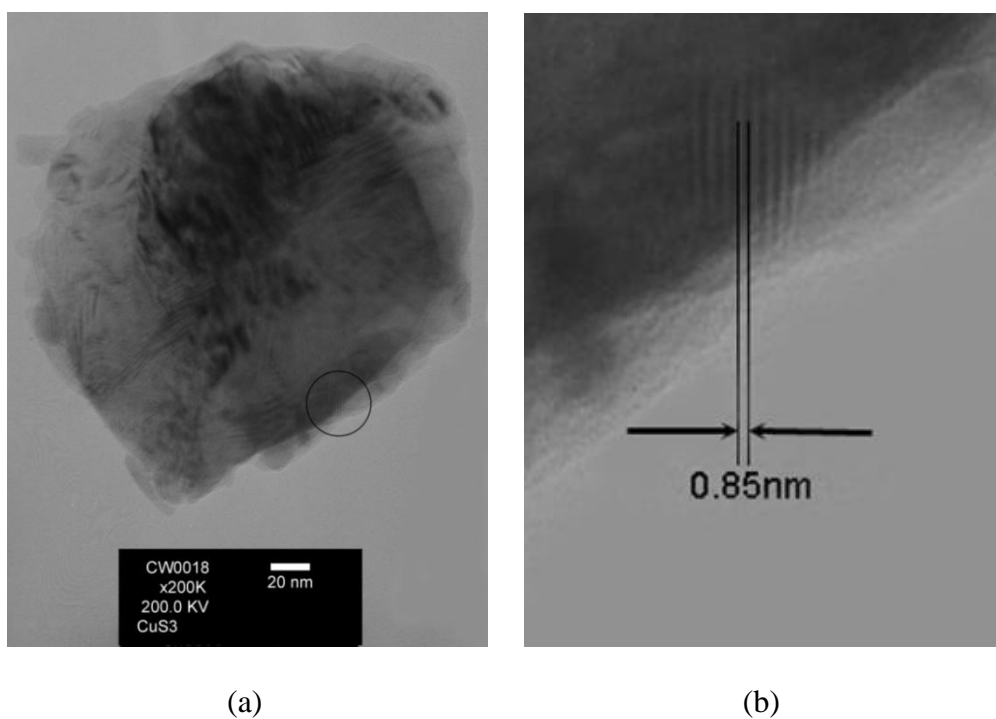
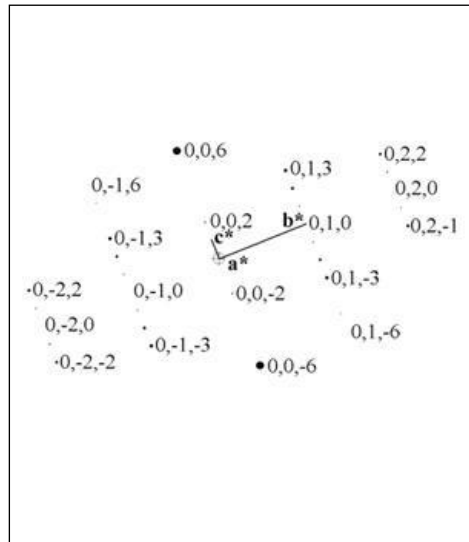


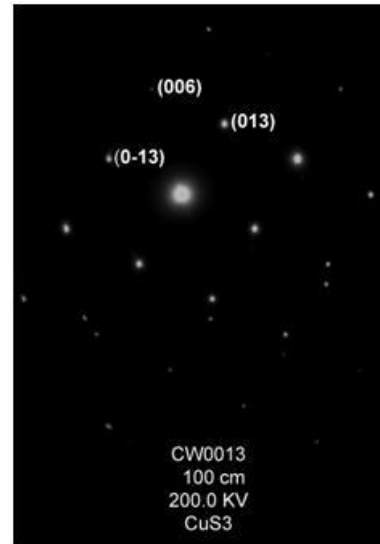
Figure 4.9 TEM images, and plane (002) of CuS produced for 5 s (a and b) respectively.

SAED patterns (Figures 4.10b and d) of single crystals with two different orientations were indexed [85], and specified as hexagonal CuS [80] with the [001]

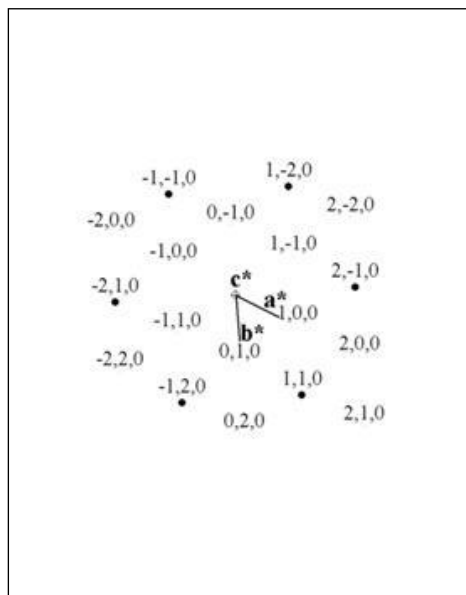
and $[-100]$ directions as the zone axes, respectively. Simulated electron diffraction patterns [86] (Figures 4.10a and c) corresponded very well with those obtained by the interpretation (Figures 4.10b and d).



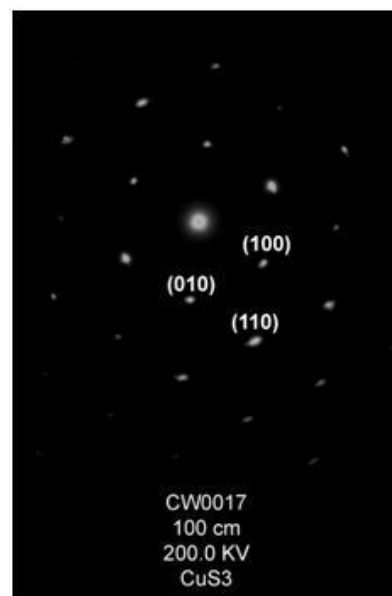
(a)



(b)



(c)



(d)

Figure 4.10 SAED simulation patterns (a and c) and HRTEM images (b and d) of CuS produced for 5 s.

4.2 AlSb synthesized via direct current heating

Conditions were operated

- Apply current 80A for 5min ; A1
- Apply current 80A for 10min ; A2
- Apply current 110A for 2s ; A3
- Apply current 110A for 3s ; A4

XRD spectra (Figure 4.11) of AlSb, produced by the direct flow of 80 A and 110 A currents through the solid mixtures for different lengths of times, were compared with the JCPDS database [80]. For A1 and A3 conditions, the products were cubic AlSb (JCPDS no. 73-2247) containing some Al and Sb impurities (JCPDS nos. 01-1176 for Al, and 02-0587 and 02-0592 for Sb). At these stages, the chemical reactions of Al and Sb are still incomplete. Upon processing at the A2 and A4 conditions, the products were pure AlSb without any impurity detection. Al and Sb completely combined together to form AlSb with cubic crystal system ($a = b = c = 6.1260 \text{ \AA}$) [80]. Comparing between the A2 and A4 conditions, the latter produced better crystalline than the former. During the direct flow of current through the solids, some Al and Sb could evaporate as well.

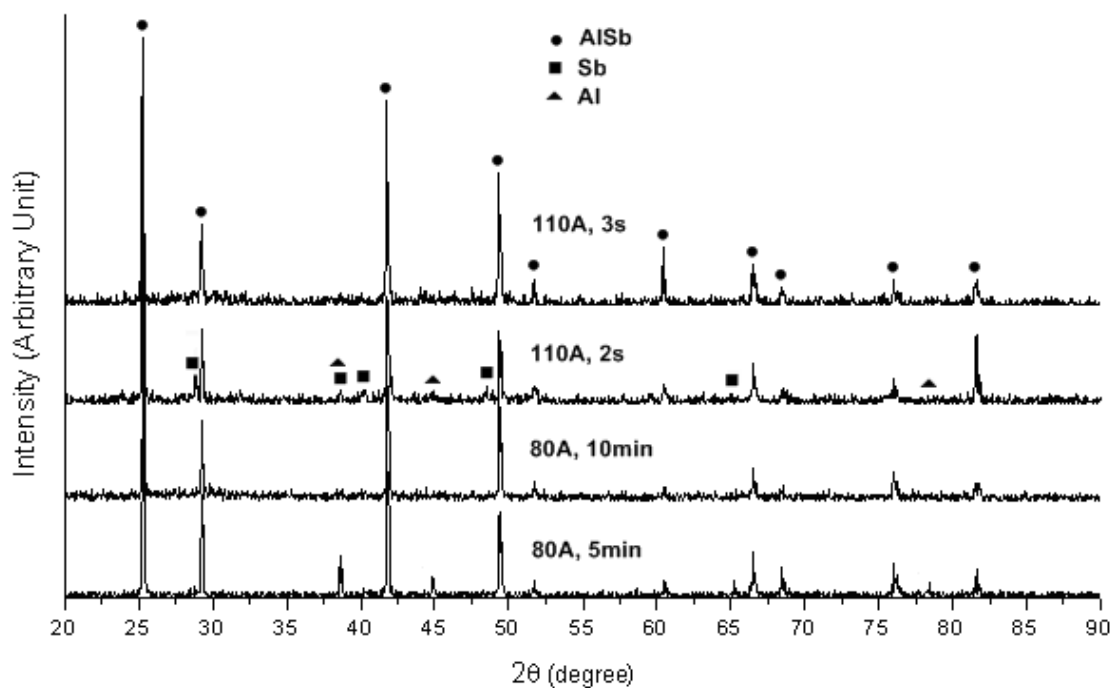


Figure 4.11 XRD spectra of AlSb produced under different conditions.

Raman spectra (Figure 4.12) show three Raman shifts at 113.3, 145.9, and 320.2 cm^{-1} , for AlSb produced at the A2 and A4 conditions. The 1st, 2nd and 3rd Raman shifts correspond very well with those characterized by Azuhata et al. – specified as the 2TA(L), 2TA(X) and TO(Γ) modes [87], respectively. No detection of any impurity peaks in these products – agree very well with the above XRD analysis. But for those produced at the A1 and A3 conditions, additional peaks at 251.9 cm^{-1} were detected. They correspond with the Raman shift of antimony, specified by RRUFF [88]. Comparing to 30 mW He-Ne laser with 632.8 nm (red) wavelength, a great deal of energy was lost during the Raman analysis, caused by the inelastic scattering process.

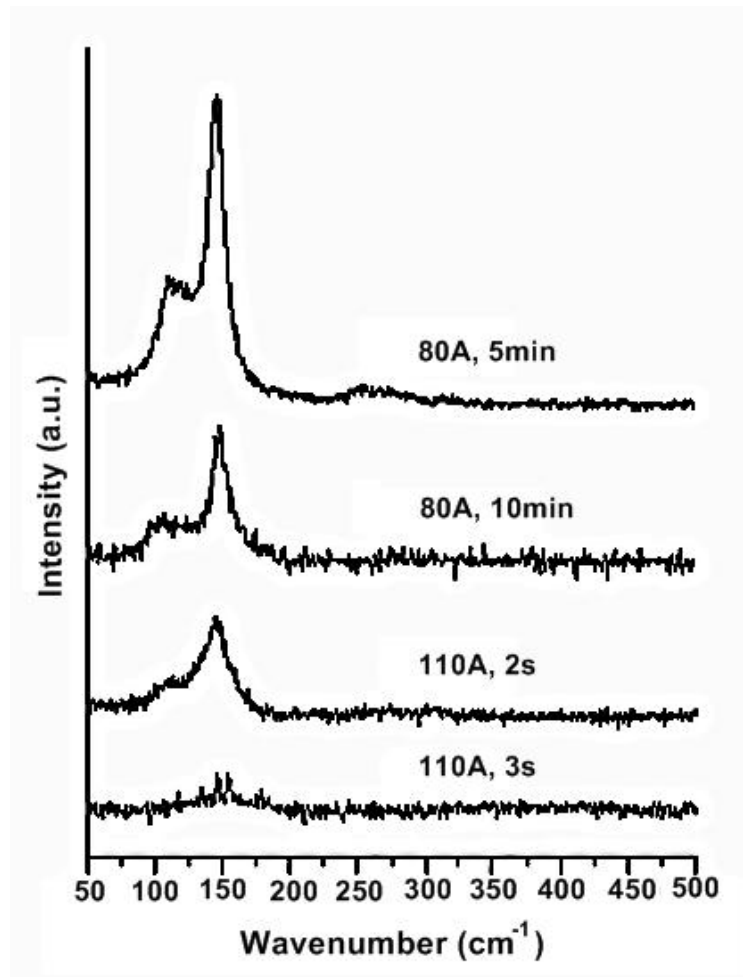


Figure 4.12 Raman spectra of AlSb produced under different conditions.

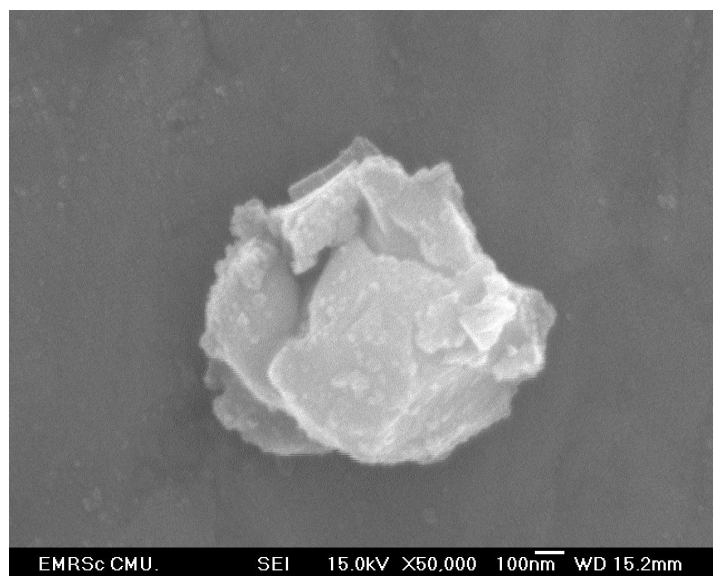


Figure 4.13 SEM image of AlSb produced at current 80 A for 10 min.

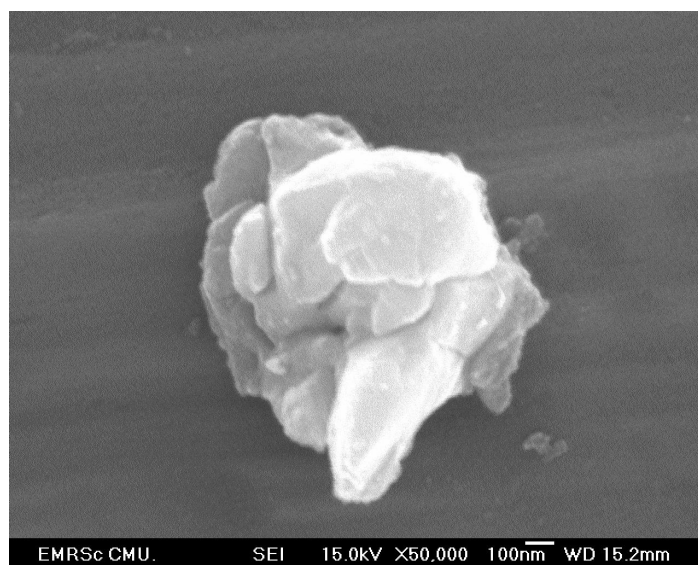


Figure 4.14 SEM image of AlSb produced at current 110 A for 3 s.

SAED patterns (Figure 4.15) of AlSb produced at the A2 and A4 conditions were indexed and interpreted [89]. Figure 4.15a and b shows several concentric rings of diffraction spots of transmitted electrons through a number of polynanocrystals with different orientations [90-93]. Figure 4.15c and e shows two SAED patterns of single crystal [92-94], and the electron beams in the $[\bar{5}36]$ and $[\bar{1}\bar{1}\bar{1}]$ directions, respectively. All these four patterns were proved that the products are cubic AlSb [80]. Diffraction patterns for AlSb with electron beams in the $[\bar{5}36]$ and $[\bar{1}\bar{1}\bar{1}]$ directions were also simulated [95], and are shown in Figure 4.15d and f. They are in symmetric and systematic order, with the a^* , b^* and c^* reciprocal lattice vectors for both patterns in the $[100]$, $[010]$, and $[001]$ directions. For one crystal structure, the corresponding reciprocal lattice vectors are the same although the electron beams are different. Comparing between the corresponding SAED and simulated patterns, they are in good accordance. Typical examples of TEM images (Figure 4.16a and b) of

AlSb produced at the A2 and A4 conditions showed that these products were composed of a number of nanograins with different orientations (50 nm and 20 nm in sizes, respectively). The XRD and SAED analyses proved that these nanograins were crystalline in nature.

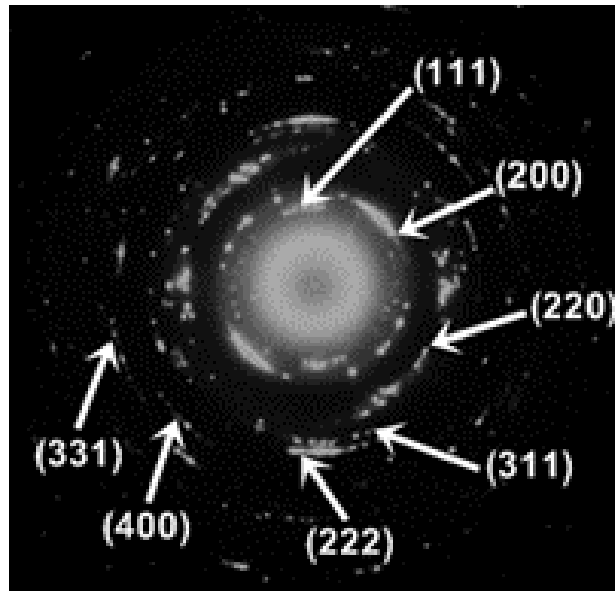


Figure 4.15a Ring diffraction pattern of AlSb produced at current 80A for 10min.

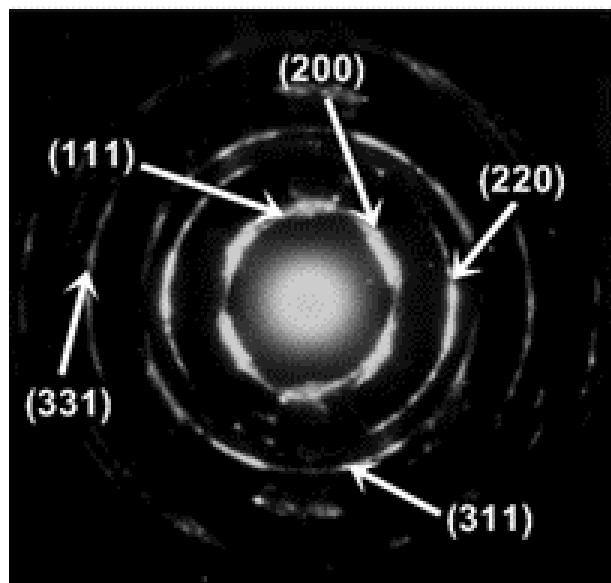


Figure 4.15b Ring diffraction pattern of AlSb produced at current 110A for 3s.

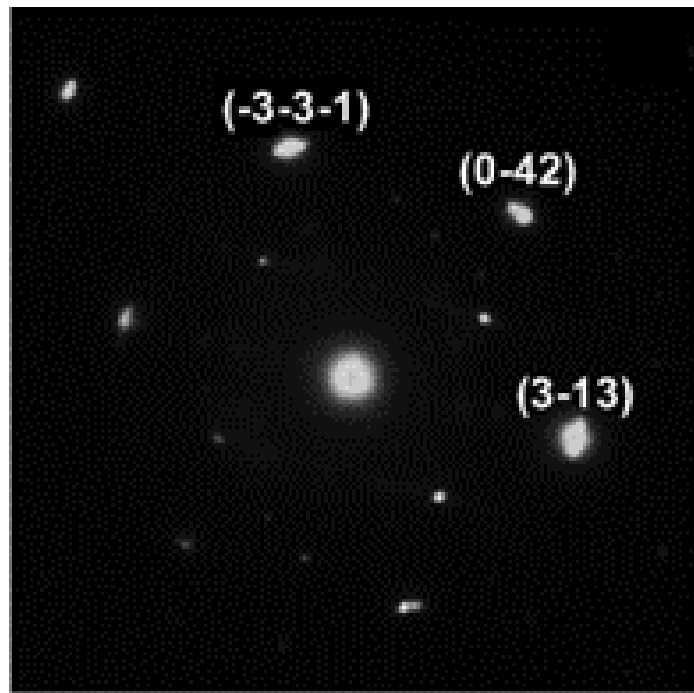


Figure 4.15c SAED pattern of AlSb produced at current 80A for 10min.

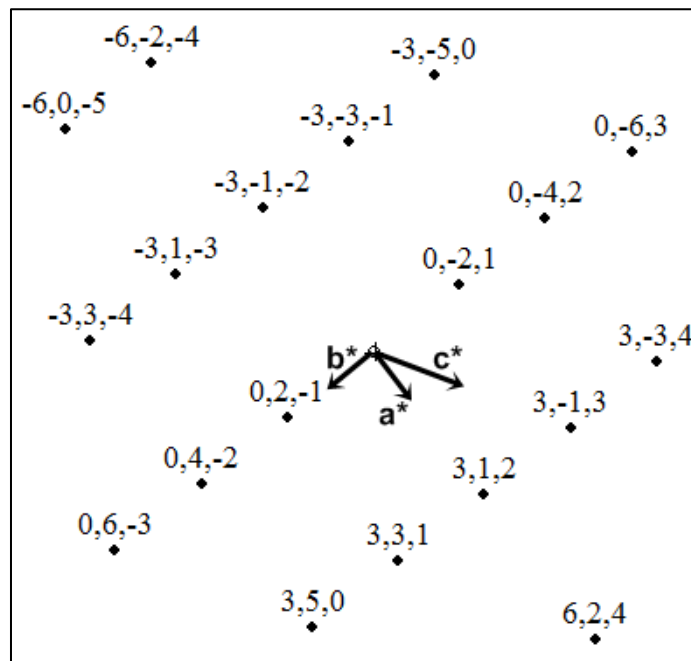


Figure 4.15d The simulated patterns of AlSb produced at current 80A for 10min.

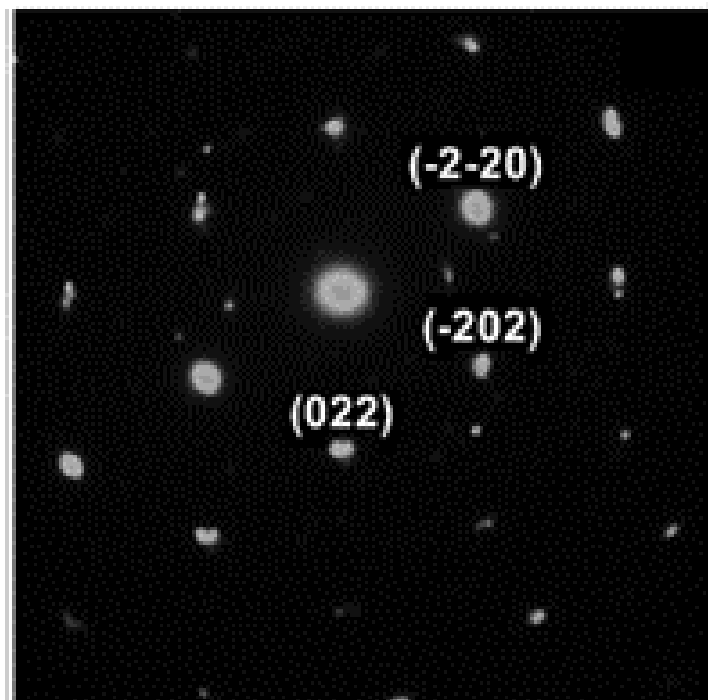


Figure 4.15e SAED pattern of AlSb produced at current 110A for 3s.

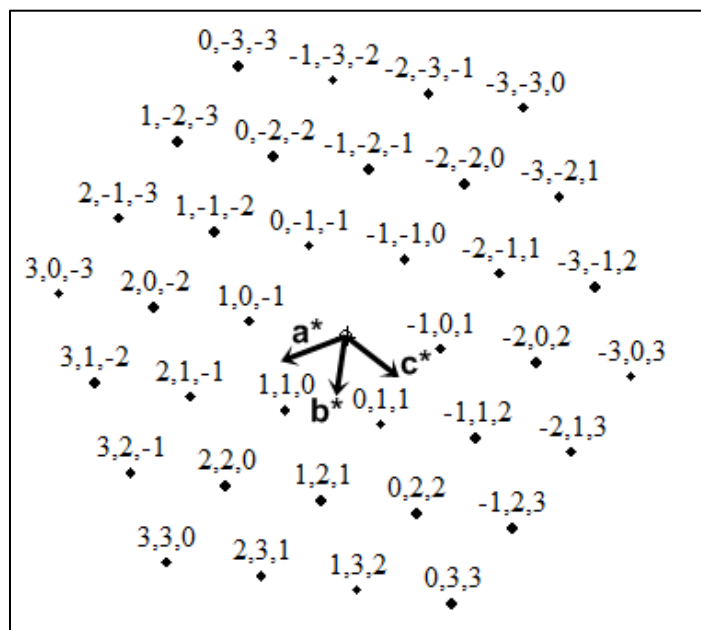


Figure 4.15f The simulated patterns of AlSb produced at current 110A for 3s.

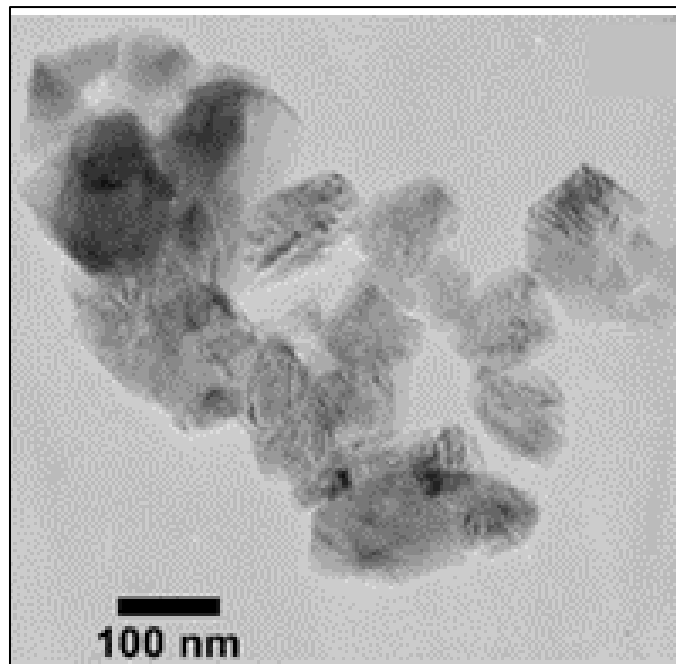


Figure 4.16a TEM images of AlSb produced at current 80A for 10min.

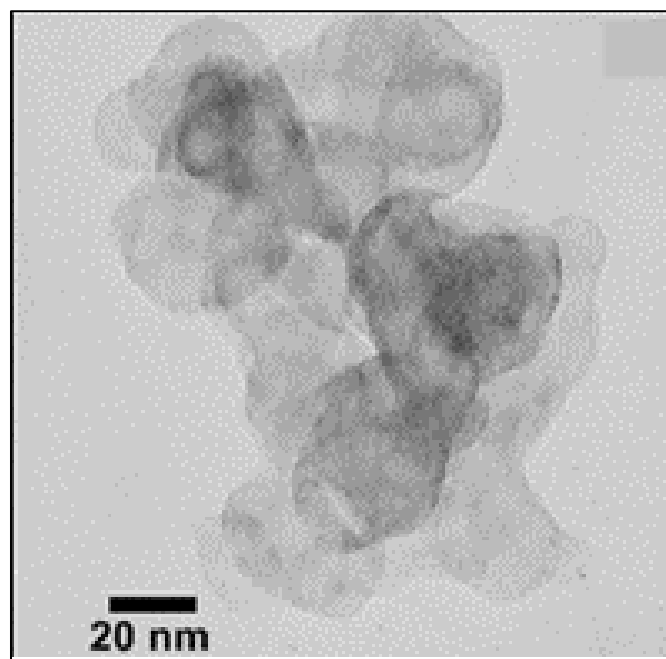


Figure 4.16b TEM images of AlSb produced at current 110A for 3s.

Absorption spectra of AlSb produced at the A2 and A4 conditions were characterized using UV-Vis-NIR spectrophotometer with the aid of the following equations [96, 97].

$$(\alpha h\nu)^{1/2} = B(h\nu - E_g) \quad (4.1)$$

$$\alpha = -(\log T)/t \quad (4.2)$$

$$t = bC/\rho \quad (4.3)$$

where α the total absorption coefficient, $h\nu$ the photon energy, B is a constant, E_g the indirect energy gap, T the transmittance of photon through the suspension in ethanol (concentration, $C = 0.001 \text{ g/cm}^3$) containing in the cuvettes (spectroscopy cells) with the path length b of 10 mm, t is the effective thickness, and ρ the density of AlSb. The curves of $(\alpha h\nu)^{1/2}$ vs $h\nu$ for indirect allowed transition were plotted (Figure 4.17), and extrapolated to $\alpha = 0$. The absorption edge energies, corresponding to the energy gaps of AlSb produced at the A2 and A4 conditions, were respectively determined [96] to be 1.647 eV and 1.688 eV, controlled by particle-sizes – energy gap increases with the decreasing in size [98] of AlSb particles. These values are in accordance with the indirect optical interband transition of AlSb reported by the research teams of Misra [99], Al-Douri [100], Anani [101], and Vurgaftman [102].

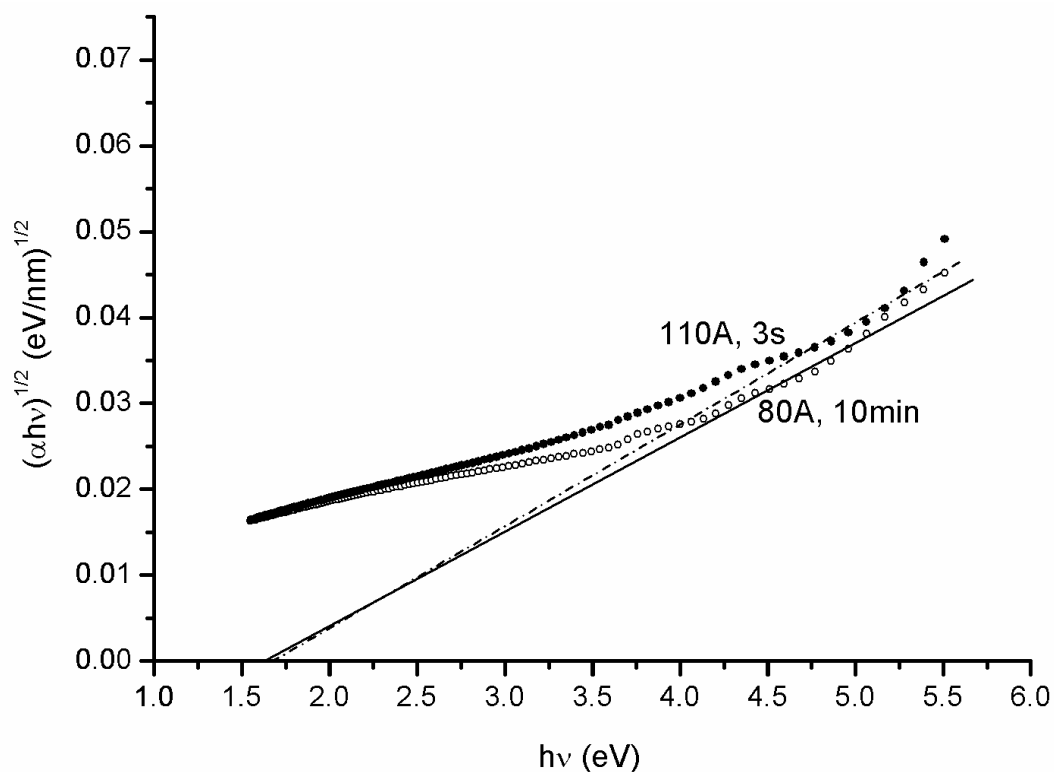


Figure 4.17 The relationship between $(\alpha h\nu)^{1/2}$ and $h\nu$ of AlSb nanocrystals produced at current 80A for 10min and current 110A for 3s conditions.

4.3 CuS-PEG composited electrolyte on quasi solid- state ZnO DSSCs

Figure 4.18 (a-c) shows XRD patterns of FTO glass and heat-treat films by microwave plasma of as-deposited Zn and calcinations of Zn to ZnO film on FTO glass, each parts show in Figure 4.19 (a-c). XRD pattern of the as-deposited film can be referred to Joint Committee on Powder Diffraction Standards [80] (JCPDS nos.77-0452 for SnO₂, 04-0831 for Zn and 89-0511 for ZnO). All the peaks of ZnO particles can be distinguished as hexagonal wurtzite structure ($a = b = 0.3249$ nm and $c = 0.5205$ nm) from the “orientation attachment” theory proposed by Penn and Banfield [103, 104].

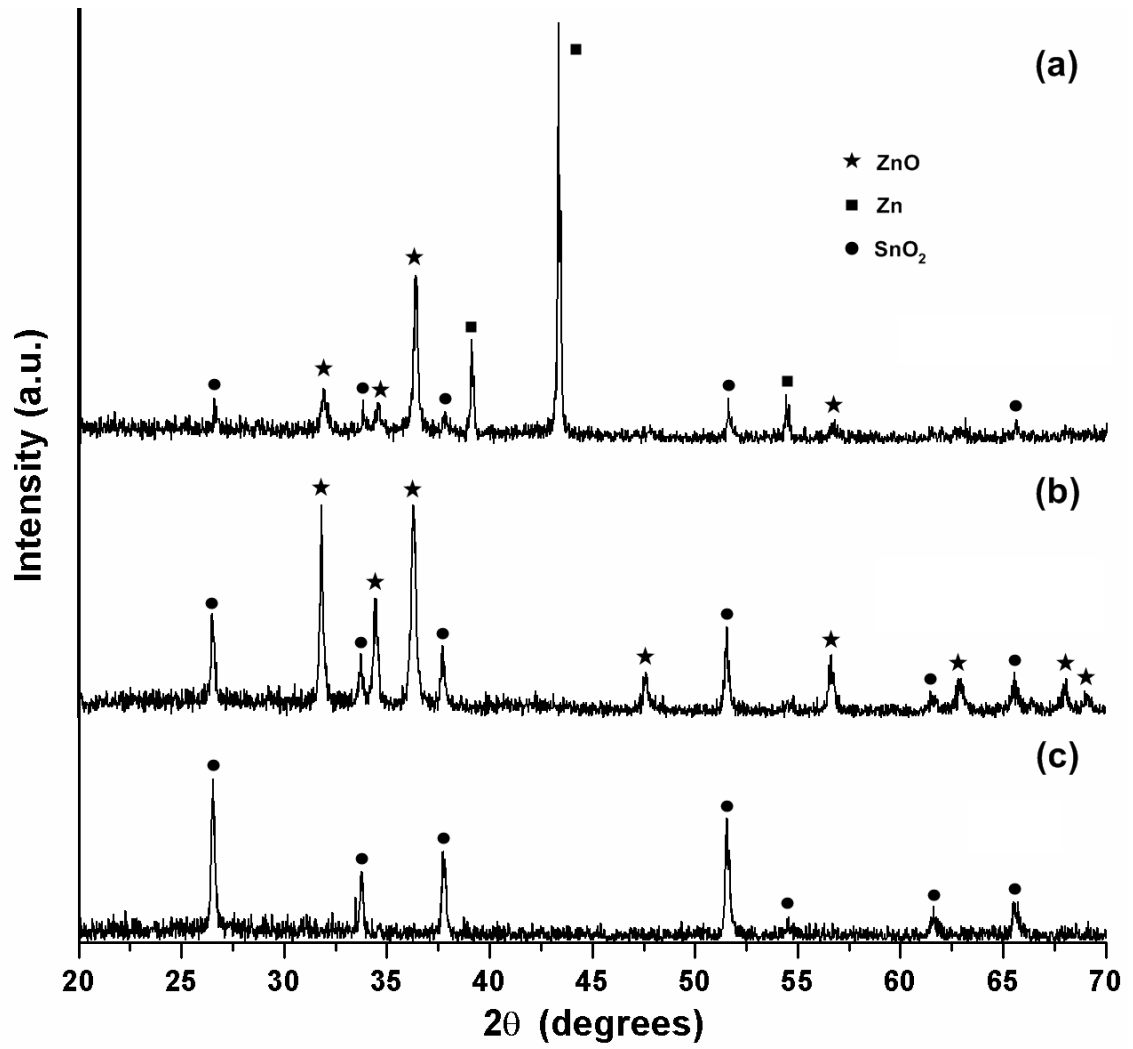


Figure 4.18 XRD patterns (a) deposit Zn film on FTO, (b) calcinations of porous Zn film to porous ZnO film, (c) FTO.

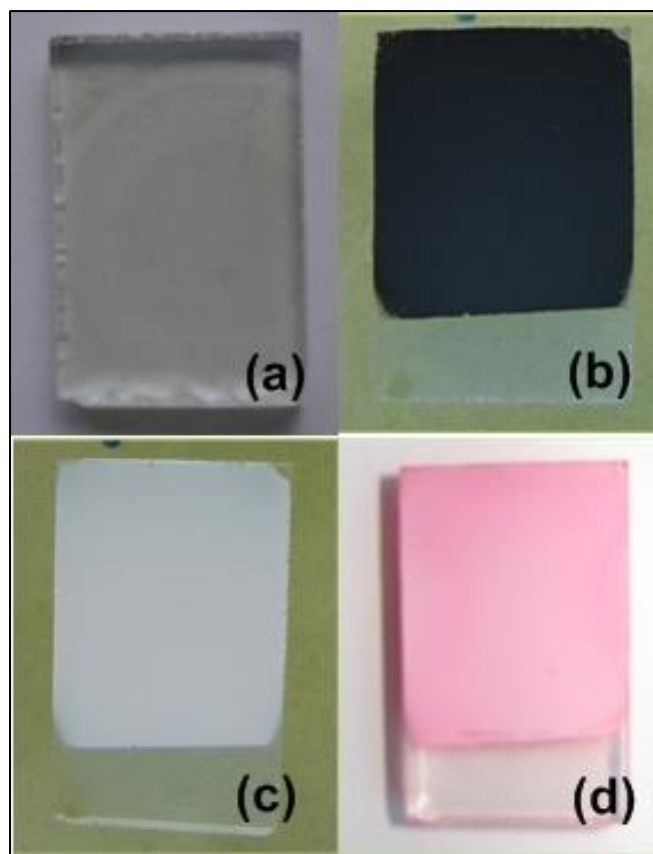


Figure 4.19 DSSC parts: (a) FTO, (b) porous Zn, (c) porous ZnO, and (d) porous ZnO after immerse with Eosin Y dye.

Figure 4.20 (a, b) show XRD patterns obtained from the experiment, and JCPDS database no. 06-0464 [80] were synthesized by using a solvothermal method [11]. The as synthesized product was a hexagonal structure covellite CuS, with no detection of any impurities. Its diffraction peaks are narrow and sharp, specifying that the X-ray radiation reflected and diffracted from atoms in lattice order.

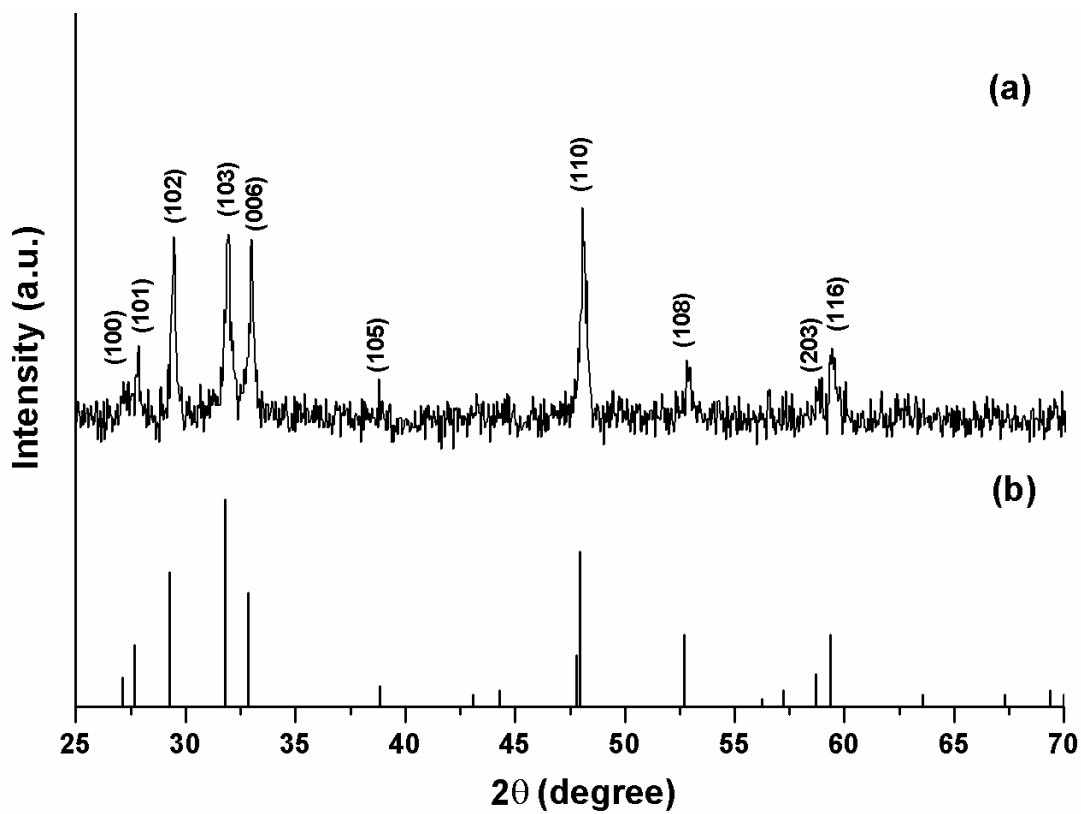


Figure 4.20 XRD pattern of the CuS (a) synthesized product produced by using a solvothermal method [11], with its patterns obtained from the, (b) JCPDS database [80].

FE-SEM and TEM pictures of the prepared ZnO film are presented in Figure 4.21 (a-f). The film is composed of agglomerate particles with an average diameter of 100 nm. The resulting films are light-scattering in the visible region due to the large particle size and ZnO film on electrodes with thicknesses about of 10 μm . Figure 4.22 show SEM picture of agglomerate CuS nanoplates and nanoparticles were prepared by using solvothermal method [11].

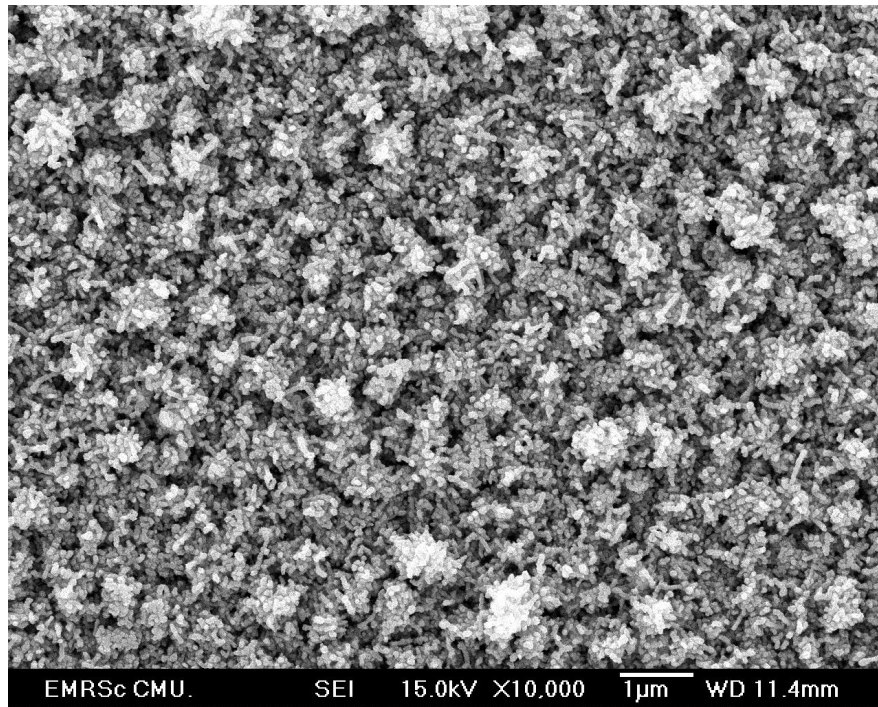


Figure 4.21a FE-SEM image of Zn particles ($\times 10,000$).

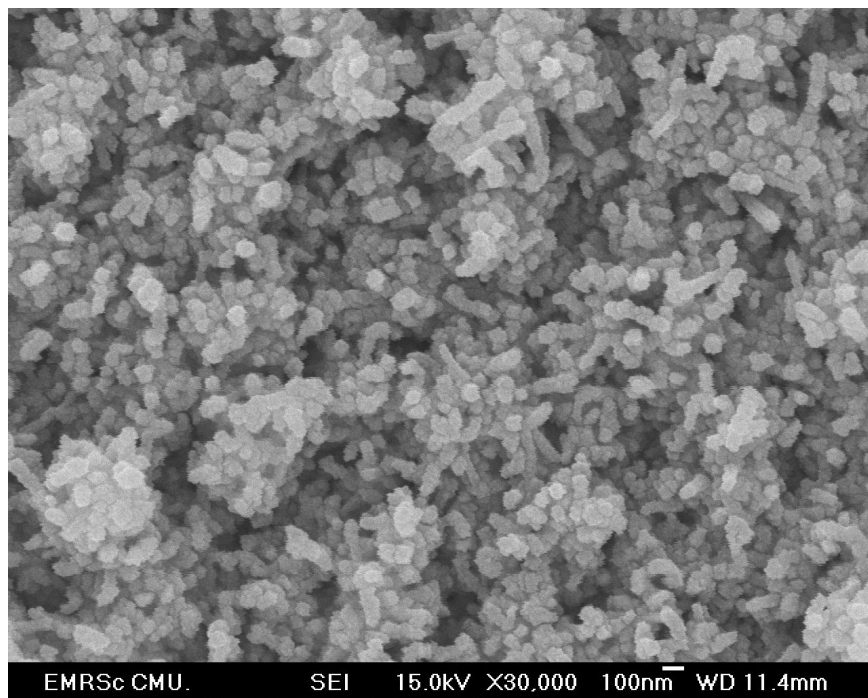


Figure 4.21b FE-SEM image of Zn particles ($\times 30,000$).

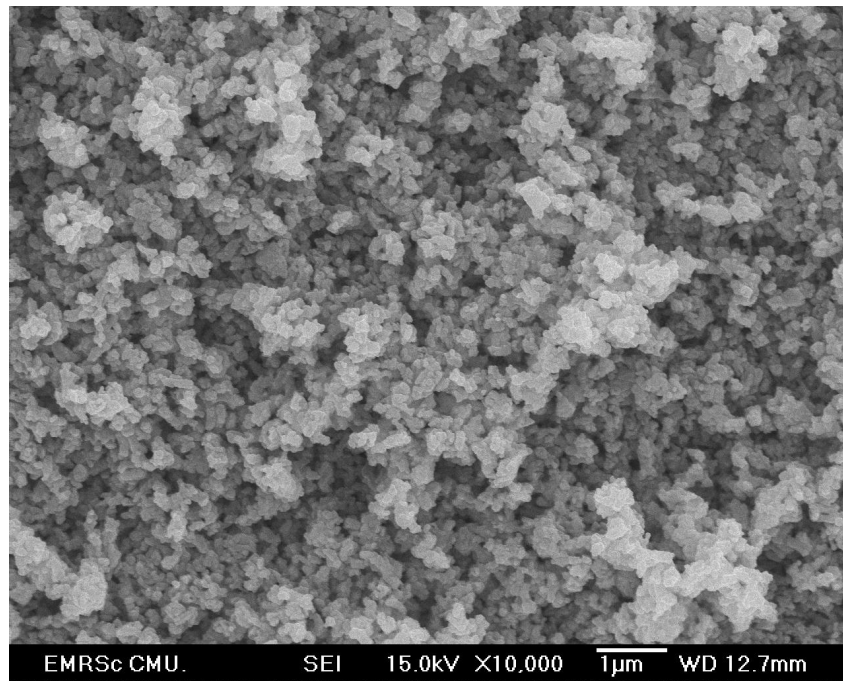


Figure 4.21c FE-SEM image of ZnO particles ($\times 10,000$).

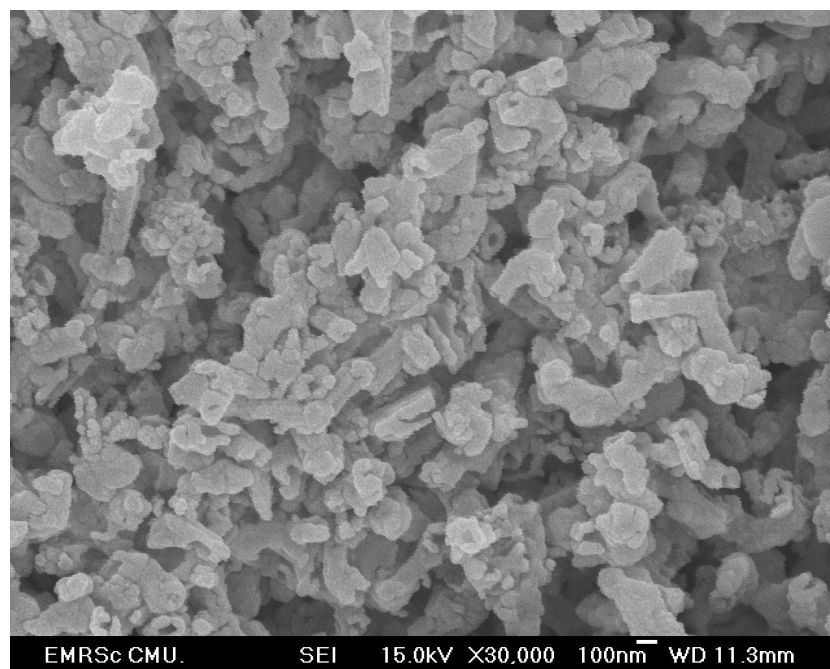


Figure 4.21d FE-SEM image of ZnO particles ($\times 30,000$).

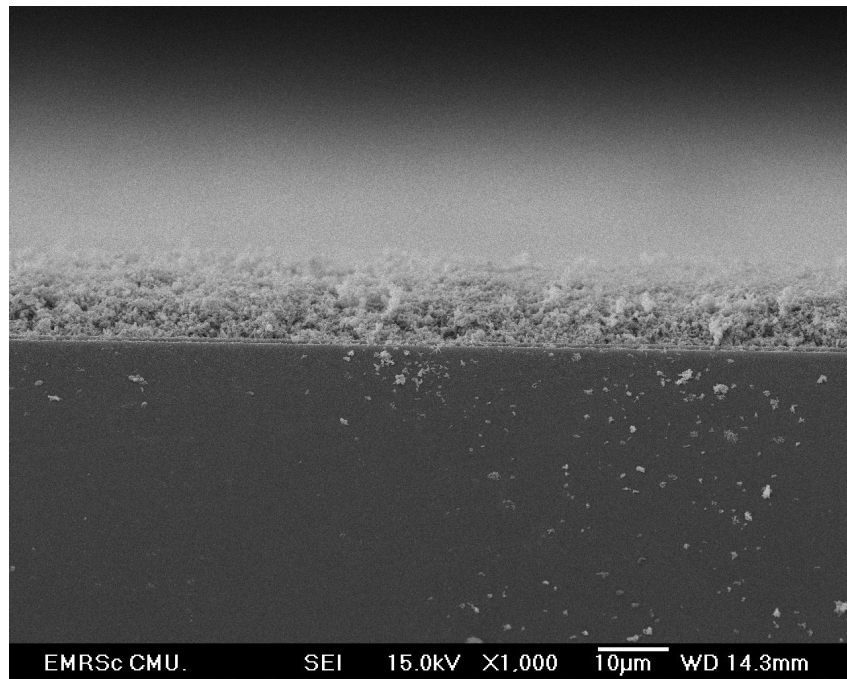


Figure 4.21e FE-SEM cross-section image of ZnO and FTO layers.

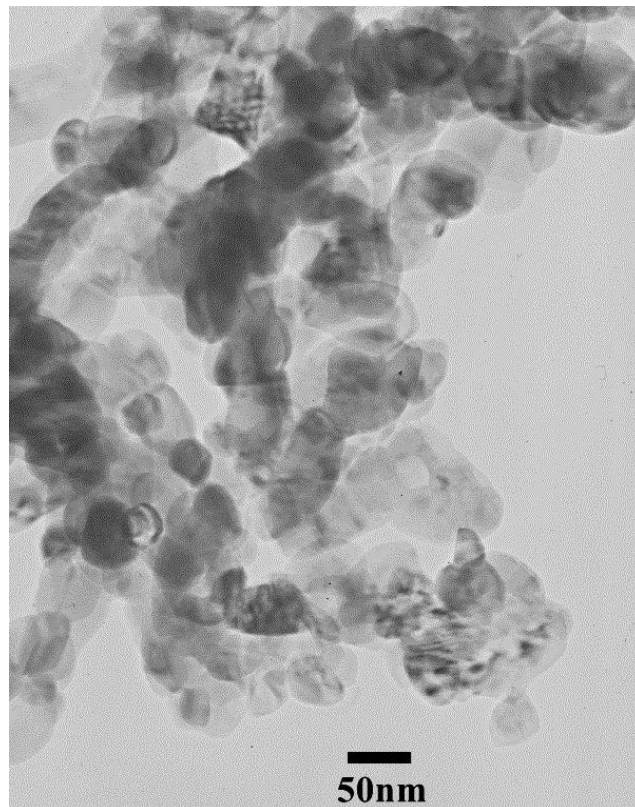


Figure 4.21f TEM image of ZnO particles.

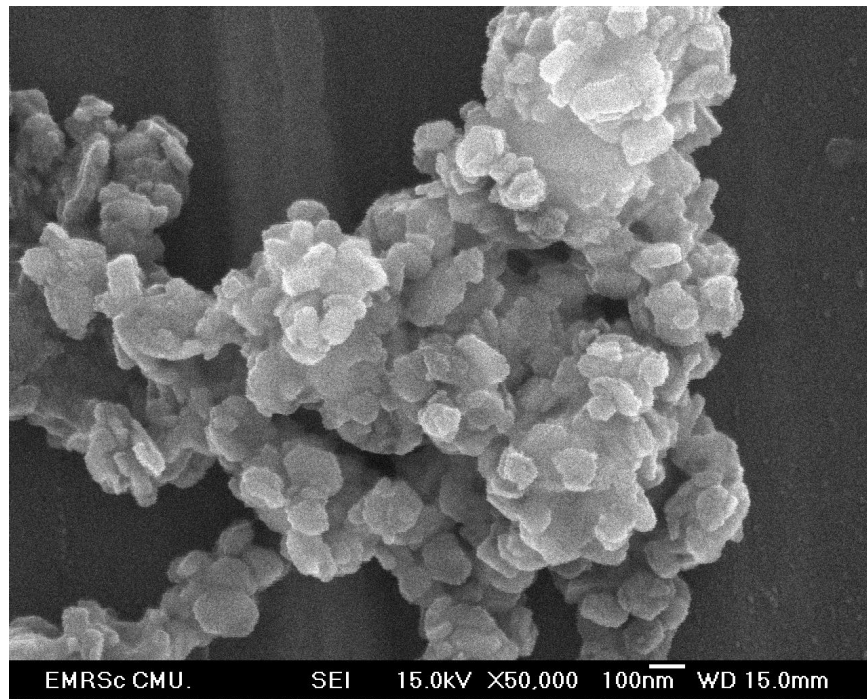


Figure 4.22 FE-SEM image of synthesized CuS by solvothermal method.

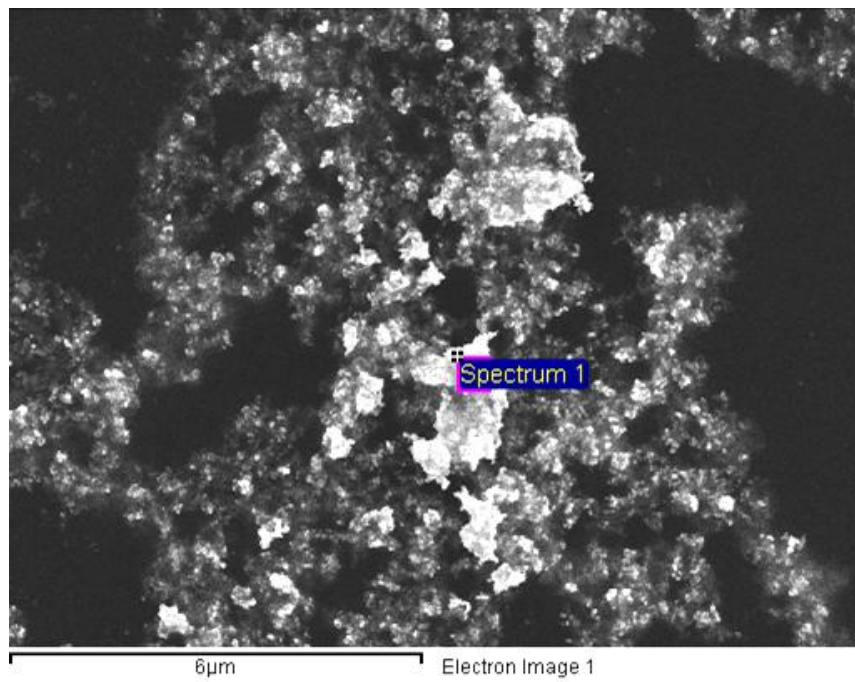


Figure 4.23a SEM-EDX image of Pt particles as catalytic.

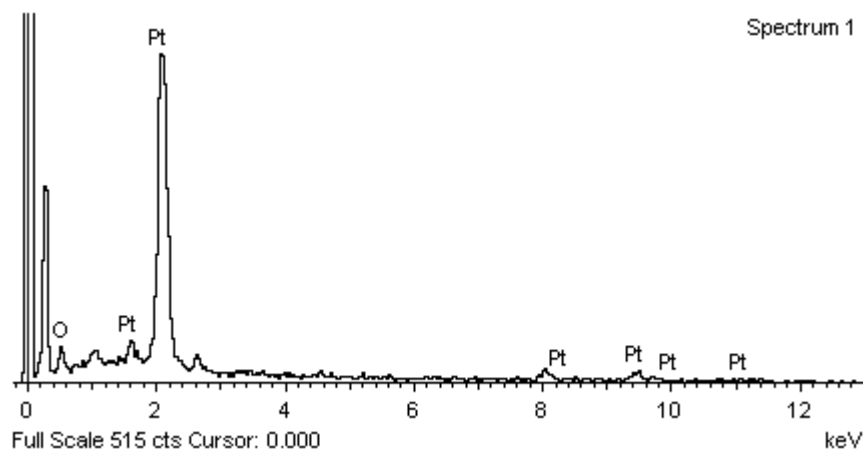


Figure 4.23b SEM-EDX Spectrum of Pt particles.

Table 4.5 Show weight and atomic percent ratio of element by EDX.

Element	Weight%	Atomic%
O K	9.61	56.46
Pt M	90.39	43.54
Totals	100.00	

UV – vis absorption spectrum (Figure 4.24) of CuS nanoplates dispersed in absolute ethanol, shows the absorption edge at 610 nm (2.03 eV). A broad absorption peak of near-IR region indicates the presence of covellite CuS, which is in accordance with those obtained by Gao et al. [105] and Guo et al. [106]. The absorbance of copper sulfide from UV–vis absorption spectrum can be used to search for optical band gaps. The optical band gaps of the copper sulfide is obtained by using the relation

from equations 3.1- 3.3 and in Figure 4.25 shows the plot of $(\alpha h\nu)^2$ versus $h\nu$, indicating a direct transition ($n = 0.5$) and extrapolated to $\alpha = 0$. This plot gives the values of the band gap to be 2.2 eV. These results are in very good agreement with the earlier report by Naşcu et al. [107], Grozdanov and Najdoski [108].

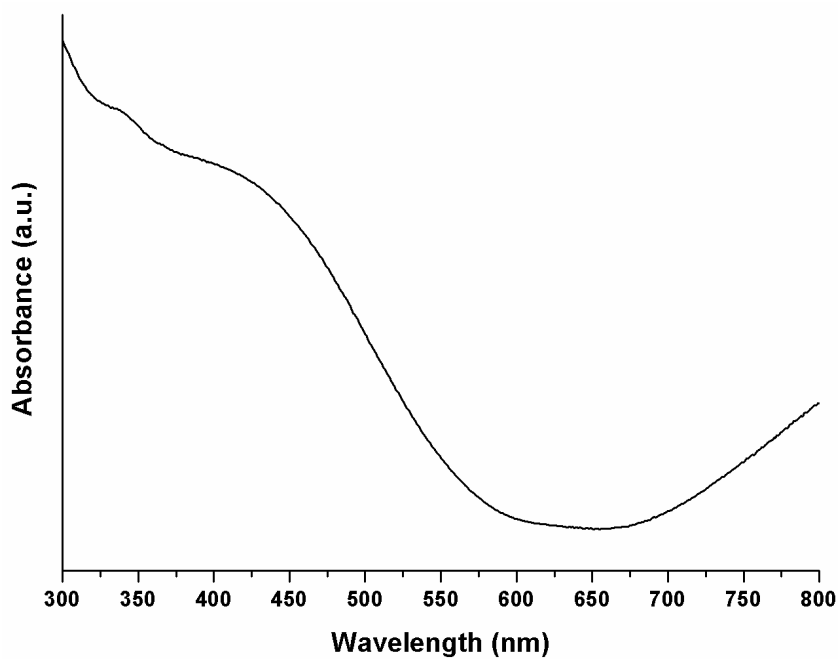


Figure 4.24 UV – vis absorbance spectrum of CuS.

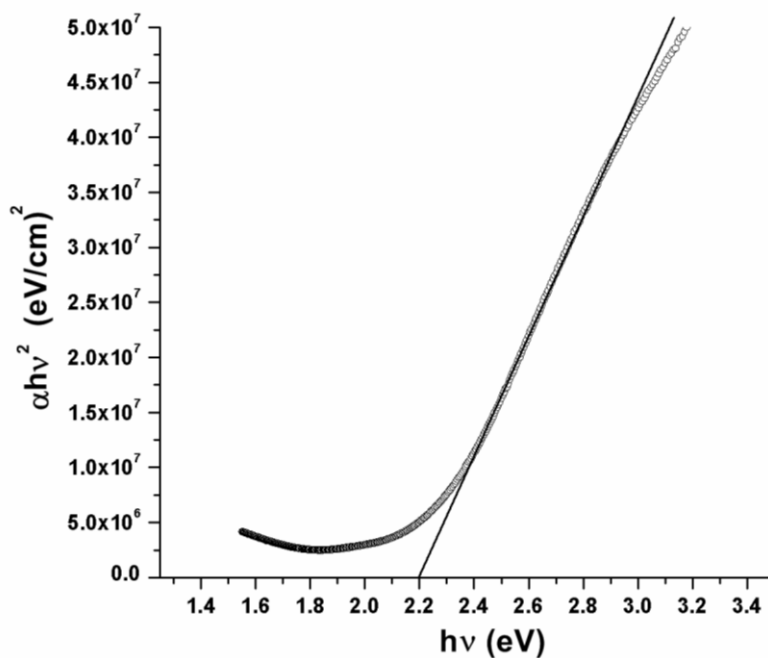


Figure 4.25 Plot of $(\alpha h\nu)^2$ versus $h\nu$ in order to obtain band gap energy of CuS.

A PL spectrum of solid CuS nanoplates (Figure 4.26) was determined using a 300 nm (4.13 eV) excitation wavelength. Its emission peak is 368.5 nm (3.365 eV), and is in accordance with the emission of CuS nanoplates at 339 nm (3.665 eV) determined by Zhang et al. [109].

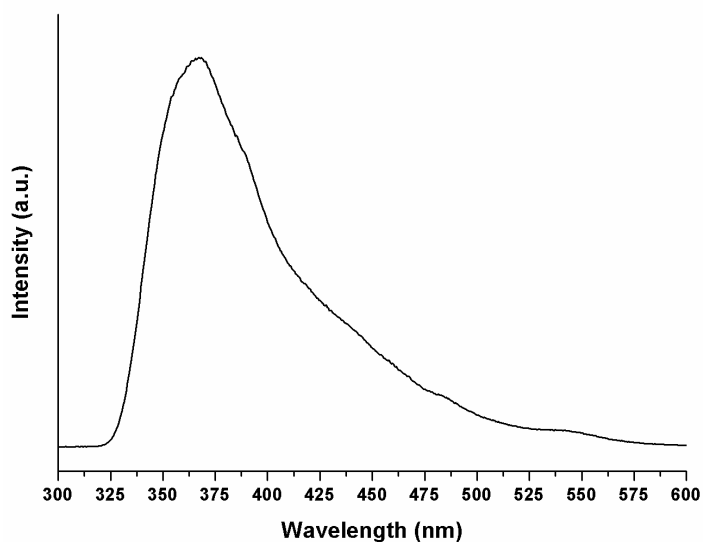


Figure 4.26 PL spectrum of solid CuS nanoplates.

The current density (J)–voltage (V) characteristics of DSSCs fabricated with PEG in comparison to different wt% CuS-PEG composite electrolytes are shown in Figure 4.27 and summarized in Table 4.6. The conversion efficiencies of DSSCs are significantly increased by using 0.5wt%CuS–PEG composite electrolytes in comparison with bare PEG. The highest conversion efficiency of 0.047 % and J_{sc} of 0.351 mA/cm². However, V_{oc} of bare PEG electrolyte is more than all of the CuS-PEG composite electrolytes. In comparison with PEG electrolyte, J_{sc} of 0.1wt%CuS-PEG is less than PEG electrolyte and increased up to 0.3wt%CuS–PEG and then still hold in 0.5wt%CuS–PEG as increasing the concentration of CuS in composite electrolyte. J_{sc} can be explained by the charge transport mechanism in I^-/I_3^- couple, which is based on the physical diffusion in electrolyte [110]. A relationship between diffusion coefficient and the limited current density (J_{lim}) is described as follows:

$$J_{lim} = \frac{2ne_o D_{I_3^-} c_{I_3^-} N_A}{l} \quad (4.4)$$

where n denotes the number of electrons transferred in the reaction (here $n = 2$), e_o the elementary charge, $D_{I_3^-}$ the diffusion coefficient of I_3^- , $c_{I_3^-}$ the concentration of I_3^- , N_A the Avogadro constant and l the distance between electrodes. In this case, the filling of CuS nanoplate into PEG matrix may be sufficiently reduced the ohmic contact to increase the electron exchange in the PEG network of electrolyte region and increased the diffusion of in the redox electrolyte. It may result the high J_{sc} less increase variation in V_{oc} of CuS-PEG. Generally, the high V_{oc} is attributed to low

recombination rate, which is accounted by low series resistance ($R_s = (dV/dI)_{I=0}$) of cell under power density of the light was adjusted to 100 mW/cm^2 (AM 1.5). The slight increase of V_{oc} as increasing CuS contents in CuS-PEG may be ascribed to the low R_s of electrodes/electrolyte due to the interference of CuS in DSSCs.

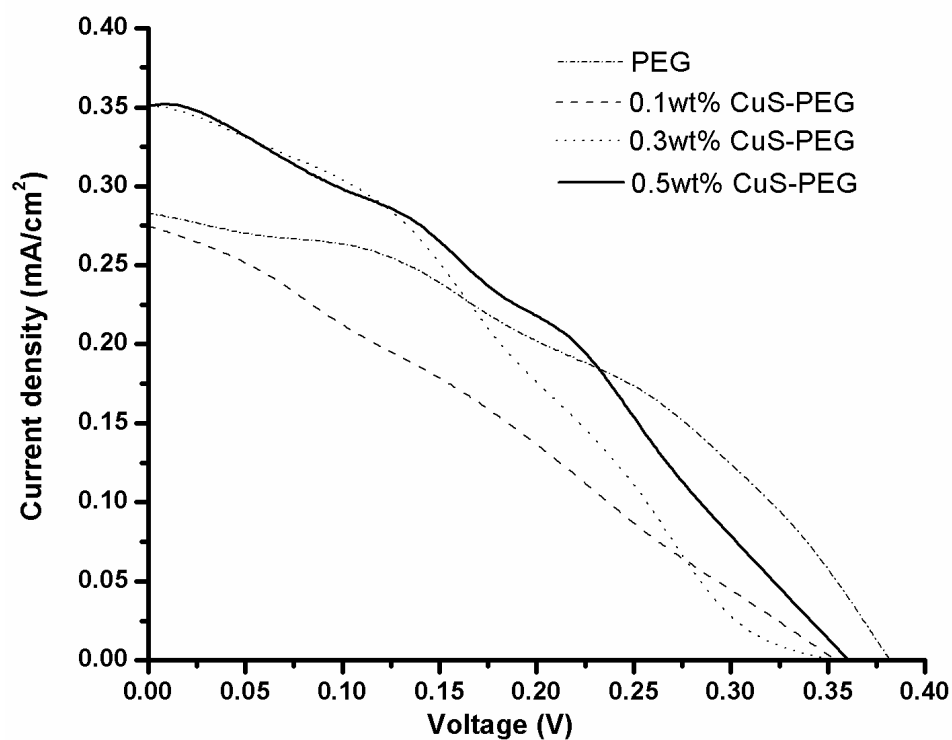


Figure 4.27 J - V characteristic curves of DSSCs in the light for different wt % CuS-PEG electrolyte.

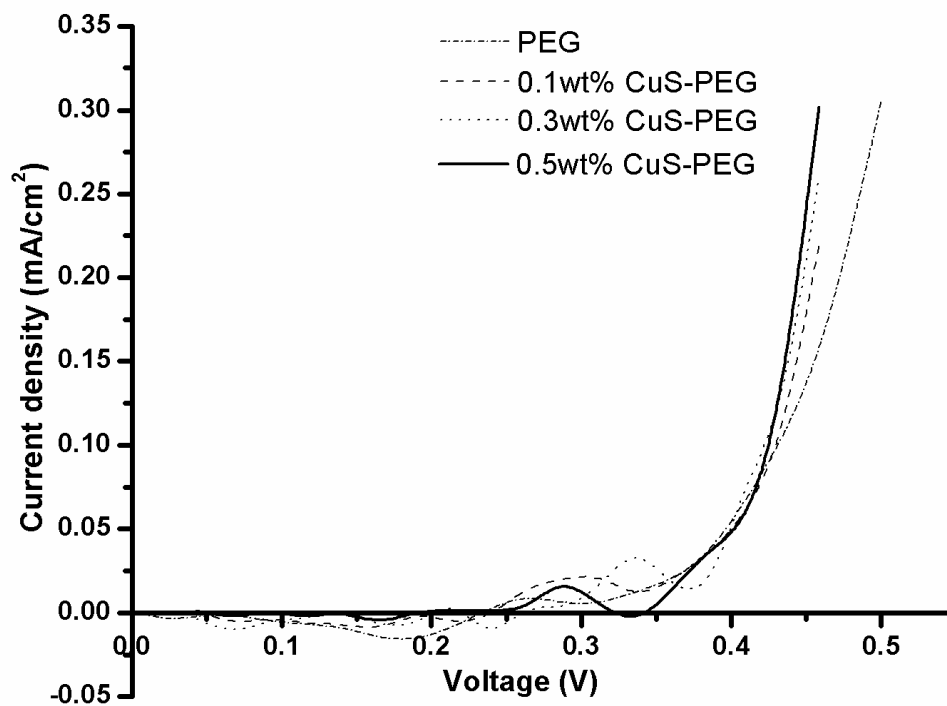


Figure 4.28 J - V characteristic curves of DSSCs in the dark for different wt % CuS-PEG electrolyte.

Table 4.6 V_{oc} , J_{sc} , FF and η for different wt % CuS-PEG electrolyte.

Electrolyte	V_{oc} (V)	J_{sc} (mA/cm ²)	FF	η (%)
PEG	0.382	0.282	0.410	0.044
0.1wt%CuS-PEG	0.355	0.275	0.288	0.028
0.3wt%CuS-PEG	0.357	0.351	0.306	0.038
0.5wt%CuS-PEG	0.361	0.351	0.369	0.047



Figure 4.29 A schematic diagram of the DSSC.



Figure 4.30 Photo of completed DSSC.